

Mesh-based vs. Image-based Statistical Appearance Model of the Human Femur: A Preliminary Comparison Study for the Creation of Finite Element Meshes

Serena Bonaretti¹, Christof Seiler^{1,2}, Christelle Boichon³, Philippe Büchler¹,
and Mauricio Reyes¹

¹ Institute for Surgical Technology and Biomechanics, University of Bern, Bern,
Switzerland

{serena.bonaretti,christof.seiler,philippe.buechler,mauricio.reyes}@istb.unibe.ch

² Asclepios Research Group, INRIA Sophia Antipolis, France

³ Ansys, Villeurbanne, France
christelle.boichon@ansys.com

Abstract. Statistical models have been recently introduced in computational orthopaedics to investigate the bone mechanical properties across several populations. A fundamental aspect for the construction of statistical models concerns the establishment of accurate anatomical correspondences among the objects of the training dataset. Various methods have been proposed to solve this problem such as mesh morphing or image registration algorithms. The objective of this study is to compare a mesh-based and an image-based statistical appearance model approaches for the creation of finite element (FE) meshes. A computer tomography (CT) dataset of 157 human left femurs was used for the comparison. For each approach, 30 finite element meshes were generated with the models. The quality of the obtained FE meshes was evaluated in terms of volume, size and shape of the elements. Results showed that the quality of the meshes obtained with the image-based approach was higher than the quality of the mesh-based approach. Future studies are required to evaluate the impact of this finding on the final mechanical simulations.

1 Introduction

Over the past years, statistical models have been introduced in computational orthopaedics as a useful investigation tool. They have been used for implant design evaluation [19,4], for fracture risk assessment [6,25] and for the discrimination of pathological from non pathological subjects [5]. The major advantage of statistical models consists in the ability of describing a dataset variations in terms of both shape and intensity. Moreover they allow creating new instances of the same dataset object, which belong to the same probability density function as the training dataset. This drives to the creation of a dense map of FE simulations and consequently a richer analysis of the bone mechanical behavior. These

characteristics have allowed overcoming one of the limitations of the studies in the field, which have been mainly performed on a small amount of data [16,13,23], limiting the generalization of these models to a complete population.

The definition of accurate correspondences is crucial for the creation of reliable statistical models [9]. For a correct modeling of both surface and volumetric information, correspondences have to be properly defined not only on the dataset object surface, but also inside the object volumes. Two different approaches exist to establish the anatomical correspondences: mesh morphing techniques and image registration techniques. In the first case, the dataset objects are represented as meshes and a chosen volume reference mesh is morphed to the other dataset [6,14]. In the second case, the dataset objects are represented by volume images and they are registered to the one chosen as reference [20,27].

Both approaches have strong features and weaknesses. The mesh-based approach provides an output that is directly compatible with finite element (FE) calculations. However, the smoothing required for the creation of well-shaped elements can penalize the accuracy of the anatomical correspondences. On the other hand, the image-based approach has no constraints related to node positioning since the FE mesh is created after the instantiation of synthetic new images. Therefore the accuracy of the correspondence establishment is less problematic for FE simulations. However, due to the nature of these techniques, the correspondence establishment at the interface background-object is more sensitive to errors as compared to pure surface-based registration techniques. Volume meshes are created separately for each instance, implying the impossibility of comparing simulation results on a element-wise basis. Finally deformation vector fields have to be invertible for the creation of new instances. To the authors' knowledge there is no study that compares the two different approaches used by the community in order to determine which is the most suitable for the creation of FE meshes.

The purpose of the paper is therefore to compare two existing methodologies which aim to create FE meshes from statistical models of appearance [10]. A comprehensive evaluation of surface or volumetric-based registration techniques is beyond the scope of this study. In the first part of this paper, we present the creation of two different pipelines, namely mesh-based and image-based. For each pipeline, starting from the same dataset, bone anatomical correspondences are determined, a statistical appearance model is built and new instances, which can be directly used for FE simulations, are created. In a second step, the quality of the FE meshes obtained with the two pipelines is compared based on common objective metrics.

2 Mesh-based and Image-based Pipelines for the Creation of FE Meshes

Two statistical appearance model approaches for the creation of finite element meshes are presented. The two approaches, namely mesh-based and image-based, had overlapping steps, as shown in Fig 1. The main difference between the two

approaches consisted in a different representation of the dataset objects. In the mesh-based approach, the bone objects were considered as meshes from the first step of the pipeline, whereas in the image-based approach they were represented by volumetric images for the whole pipeline. In this case, the images were transformed to FE meshes in the very final step. For completeness and reproducibility purpose, details about data and implementation can be found in Appendix A.

Segmented CT images were the input for both pipelines. Mesh morphing and image registration were used to find anatomical correspondences, respectively for the mesh-based and the image-based approaches. For both the mesh-based and the image-based pipelines, the same principals were used to calculate the statistical appearance models and to create new instances.

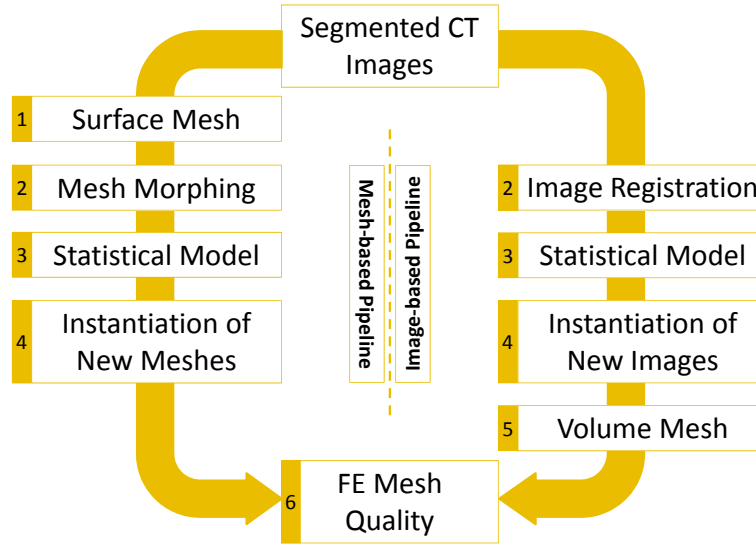


Fig. 1: Mesh-based and image-based statistical appearance model pipelines for the creation of femur finite element meshes. On the left side, the steps for the mesh-based approach are shown, whereas on the right side the steps for the image-based pipeline are depicted.

1. Surface Mesh Creation. In the mesh-based pipeline, for each bone of the dataset a surface mesh was created following the steps shown in Fig. 2. From each segmented CT image (Fig. 2a), a surface mesh was created using the marching cube algorithm [17] (Fig. 2b). The obtained mesh resulted too dense and rough and could not be directly used for the following processing. Therefore, in order to improve the mesh quality, each mesh was decimated and smoothed using the Laplacian operator. Since in many cases the node removal

caused the loss of mesh topology, node connections were reestablished using MRFSurface [18] (Fig. 2c).

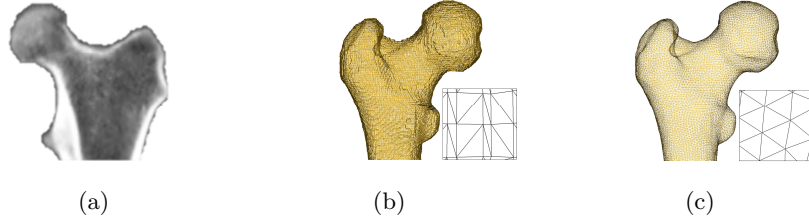


Fig. 2: Creation of femur surface mesh from CT image. (a) Sagittal view of a segmented femur head CT image. (b) Surface mesh obtained from the marching cube algorithm. (c) Surface mesh topology reconstruction.

2. Finding Correspondences: Mesh Morphing and Image Registration. In order to find anatomical correspondences among the dataset objects, mesh morphing was used for the mesh-based pipeline, whereas image registration was performed for the image-based approach. In both cases, correspondences were calculated with respect to the same reference bone. The choice of the reference bone was done in the image-based pipeline using an iterative procedure. In the first step, one bone of the dataset was randomly picked as the reference and all the remaining bones of the dataset were registered to it. The average transformation was then calculated and the bone whose transformation was the closest to the average transformation was considered as the new reference femur. These steps were repeated until convergence.

The mesh morphing was performed using the algorithm developed by [15] and extended by [3]. First, a volumetric mesh was created for the reference bone. From the surface mesh, the volume mesh was created using NETGEN [24]. The reference volumetric mesh was composed of 130000 quadratic tetrahedrons, in order to satisfy the necessary level of mesh refinement for femur FE simulations [28]. Then, the reference bone volumetric mesh was warped to all dataset surface meshes to create iso-topological tetrahedral FE meshes. To compute the mesh morphing, 10 landmarks were manually selected on the surface of both the reference volume mesh and the bone dataset surfaces meshes, as shown in Fig. 3. Four landmarks were selected in correspondence to the main anatomical features of the femur head (Fig. 3a) and 6 at easily detectable points in the condyle area (Fig. 3b). The landmarks were used as constraints during the morphing computations. The mesh morphing was executed first on the surface mesh and then on the volume mesh. From the reference volume mesh, the surface mesh was extracted. For each bone, both the reference surface mesh and the current bone surface mesh were projected on a disc of unitary radius. The position of the bone landmarks with respect to the reference bone landmarks was used as constraint for the moving of all bone surface nodes. The new position of the femur surface

nodes was then calculated using radial basis functions (RBF), where the center of the functions was represented by the landmarks. The bone surface nodes were then reprojected back from the parametric space to the physical space, and their positions smoothed. As second step, the reference volumetric mesh was morphed to the current bone new surface mesh. The position of the volumetric mesh inner nodes was calculated using RBF. In this case, the RBF center was represented by the just computed surface nodes.

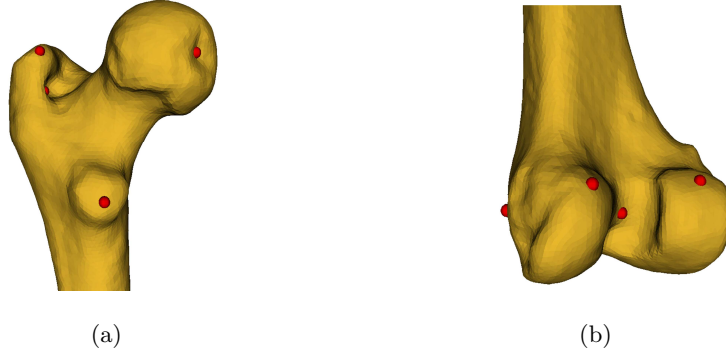


Fig. 3: Landmarks selection for mesh morphing. (a) Selection of four landmarks in the femur head. (b) Selection of six landmarks in the femur condyles (two landmarks not visible).

In the image-based pipeline, correspondences were detected using image registration. We used the Log-Domain Demons (LDD) registration algorithm regularized with a femur-specific polyaffine model [26]. The LDD finds Deformation Vector Fields (DVF) which are smooth and invertible [27]. This characteristic enables the creation of new instances, as explained in Section 2.4. In the LDD, DVF are generated through the exponential of Stationary Velocity Fields (SVF), which are the primary results of the registration process [2]. The LDD iteratively minimizes the energy functional composed of two terms, namely the ‘correspondence’ term, which calculates the SVF and the ‘regularization’ term, which imposes smoothness on the SVF [7]. In our case, the regularization term was replaced by a polyaffine model, which allowed us to capture the main anatomical variation of the femur. In the model, three regions were defined: femur head, shaft and condyle area. The parameters of the polyaffine model were jointly estimated using a closed form least square solution during each iteration step of the LDD.

3. Statistical Models. The statistical appearance model was created as a combination of the parameters obtained from the statistical shape model and the statistical intensity model [10].

In the mesh-based approach, the *statistical shape model* was computed on the volume mesh coordinates. In order to calculate the principal component

analysis (PCA), the volume meshes were aligned to the average mesh using the Procrustes method [11]. The model was then built on the aligned meshes [9]. In the image-based approach, instead, the statistical shape model was computed as a statistical deformation model [21]. Therefore PCA was directly calculated on the SVF obtained from the image registration process.

For the mesh-based approach, the *statistical intensity model* was created on the image intensity values at the corresponding mesh node positions. For the creation of valid FE meshes, the assignment of correct grey levels to the mesh nodes is crucial. In fact CT information and bone mechanical properties are strictly linked [22]: CT image grey levels represent the bone mineral density [8], which is related to the Young's modulus through empirical relationships [12]. One critical aspect affecting the Young's modulus assignment is the partial volume effect that occurs on the bone surface [13]. Therefore the bone outer layer was first eroded to delete the partial volume effect area and then dilated to rebuild the canceled outer cortical bone. At each node of the mesh, intensities were calculated as a 26-voxel connectivity linear interpolation. The computed intensities were finally used for the PCA calculation. On the other side, for the image-based approach, the statistical intensity model was created through the calculation of the PCA on the original images warped to the reference bone in order to have spatial correspondence among the gray levels of the dataset images.

For both the mesh-based and the image-based approaches, the *statistical appearance model* was built on the combination of shape and intensity parameters, as shown in Eq. 1.

$$b = \begin{pmatrix} W_s b_s \\ b_g \end{pmatrix} = \begin{pmatrix} W_s \Phi_s^T (x - \bar{x}) \\ \Phi_g^T (g - \bar{g}) \end{pmatrix}, \quad (1)$$

where b represents the combined parameters, composed by the shape parameters b_s and the intensity parameters b_g ; Φ_s^T and Φ_g^T represent respectively the transposition of the modes calculated from the statistical shape model and the statistical intensity model; x and g are the initial mesh coordinate and intensity dataset; \bar{x} and \bar{g} are the average shape and intensity, respectively. Since the shape and the intensity parameters were represented by different units, the shape parameters were multiplied by the matrix W_s in order to make the parameters homogeneous. W_s was calculated as $W_s = rI$, where r is the square root of the ratio between the total variation obtained from the statistical intensity model and the total variation calculated from the statistical shape model, and I is the identity matrix.

4. Instantiation of New Samples. For both the mesh-based and the image-based pipelines, new instances were created from the statistical appearance model. The new shape \tilde{x} was created using Eq. 2 and the corresponding intensity distribution \tilde{g} using Eq. 3:

$$\tilde{x} = \bar{x} + \Phi_s W_s^{-1} \Phi_{c,s} c \quad (2)$$

$$\tilde{g} = \bar{g} + \Phi_g \Phi_{c,g} c, \quad (3)$$

where

$$\Phi_c = \begin{pmatrix} \Phi_{c,s} \\ \Phi_{c,g} \end{pmatrix}, \quad (4)$$

represents the combined eigenvectors derived from the calculation of PCA on the combined parameters b , divided in its shape component $\Phi_{c,s}$ and intensity component $\Phi_{c,g}$. The parameter c was calculated as $-2\sqrt{\lambda_i} \leq c \leq +2\sqrt{\lambda_i}$, where λ_i is the current eigenvalue, whereas the weight between -2 and $+2$ was calculated using the latin hypercube sampling method.

In the mesh-based approach, the new shape was built assigning to the reference topology the new node coordinates. The calculated gray levels were then associated to the mesh nodes. In the image-based pipeline, the new image intensity were calculated in the reference shape. The obtained image was then warped to the new shape calculated, thanks to the invertibility of the Demons DVF.

5. Volume Mesh Creation. At the end of the image-based approach, for each new instance, a FE mesh was created. Similar to the processing performed in steps 1 and 2, from each new image, a surface mesh was created using the marching cubes algorithm. To ensure good mesh quality, the mesh was then simplified and smoothed, and its topology reconstructed using MRFSurface. Finally from the obtained surface mesh, a tetrahedral quadratic FE mesh of about 130000 elements was created using NETGEN.

6. FE Mesh Quality Assessment. Three different criteria were used to evaluate the quality of the finite element meshes. We evaluated mesh elements in terms of volume, size and shape, using the following metrics:

- a Jacobian. It is a volume metric which describes the distortion of the element from the ideal shape. At its extremes, $+1$ and -1 , the element shape was considered perfect and distorted, respectively; at 0 the element had null volume.
- b Edge ratio. It is a size metric which is calculated as the ratio between the longest and the shortest edge of the element.
- c Minimum angle. It is a shape metrics that evaluates the smallest angle of the element sides.

3 Experiments on Femur CTs

To compare the two pipelines, we conducted calculations on left femur bone CT images. In the following paragraphs we show the results that we obtained for the steps of the pipeline. The numbering of the steps refers to Fig 1.

Finding Correspondences: Mesh Morphing and Image Registration (step 2). A total of 196 segmented CT images were used in this study. According to a visual evaluation, mesh morphing failed for 25 meshes, whereas image registration failed for 24 images. Both mesh morphing and image registration

succeeded in 157 cases, which were considered as input dataset for the statistical appearance models.

Statistical Models (step 3). The results of the statistical appearance models are shown in Table 1. The variations of the dataset were described in a more compact way by the model obtained with the mesh-based approach than with the image-based approach (Table 1a). The evaluation of the computational time showed that the mesh-based approach was less time and memory consuming than the image-based one, even on a less powerful machine (Table 1b). In the mesh-based pipeline, computations were done in a few minutes, whereas hours of calculations were required in the image-based pipeline.

Table 1: Statistical appearance model computation results. (a) Model compactness for the mesh-based and the image-based pipelines. (b) Computational costs for the calculations.

(a)		
model compactness	mesh-based pipeline (# modes)	image-based pipeline (# modes)
50%	2	3
75%	6	27
80%	10	41
90%	40	86
95%	75	117
100%	157	157

(b)		
	mesh-based pipeline	image-based pipeline
Shape Model	5 min ¹	5 hrs ²
Intensity Model	2 min ¹	1.5 hrs ²
Appearance Model	9 min ¹	6.5 hrs ¹

¹ Processor: Intel Core Duo, E8500 @ 3.16GHz. RAM: 8GB

² Processor: Intel Xeon CPU, X5550 @ 2.67GHz. RAM: 48GB

Instantiation of New Samples (step 4). A total of 30 new instances were created for each pipeline. In order to create samples that represented the 90% of variation of the population, 40 modes were used for the mesh-based approaches, whereas 86 modes were used for the image-based approach.

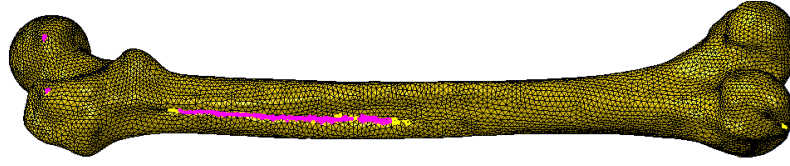
FE Mesh Quality Assessment (step 6). The evaluation of the mesh element quality resulted as follows:

- a Jacobian. Two of the 30 meshes created with the mesh-based pipeline had respectively 1 and 64 elements with a zero or negative Jacobian (Fig. 4a). None of the 30 volume meshes created with the image-based pipeline had distorted elements.
- b Edge ratio. For the meshes created with the mesh-based pipeline, both the average and the standard deviation of the edge ratio were greater and spread in a wider range than for the image-based approach (Fig. 4b). One mesh had 2 elements whose edge ratio was greater than 10 [1], therefore the mesh could not be used for FE calculation. For the image-based pipeline, meshes had a smaller edge ratio with less variations.
- c Minimum angle. As for the previous metric, for the meshes created with the mesh-based pipeline, the minimum angle results were more spread than for the meshes created with the image-based approach (Fig. 4c). Moreover, the meshes created with the mesh-based approach had a smaller minimum angle with larger variations. Six meshes had from 1 to 37 elements whose minimum angle was less then 10 degrees [1], compromising the meshes usability in mechanical simulations.

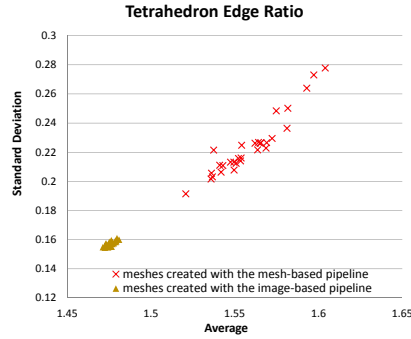
4 Conclusion

In this study we presented a preliminary comparison between two existing different statistical appearance model pipelines for the creation of FE meshes, namely a mesh-based and an image-based approaches. The mesh-based pipeline allowed the calculation of a more compact statistical model of appearance and the direct creation of iso-topological meshes as output of the statistical model. On the other hand, in the image-based approach the correspondence among mesh elements is lost since each mesh is created separately. Moreover the image-based approach is computational expensive and has the issue of the inversion of the DVF for new instances creation. In both pipelines, the ability of the models at describing the training dataset variation resulted to be similar. However the quality of the mesh tetrahedrons created with the image-based pipeline was higher. Image-based pipeline meshes performed better in terms of element distortion, size and shape.

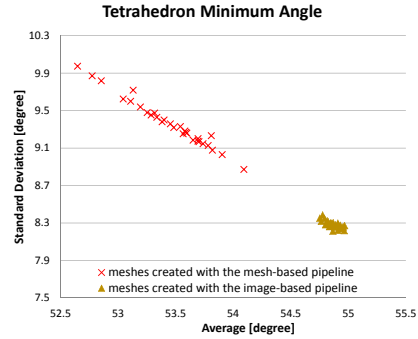
Future work is required to merge the strengths of both pipelines, to compare the mechanical properties assignment in the two approaches and to evaluate the implication for finite element simulations.



(a)



(b)



(c)

Fig. 4: FE mesh quality assessment. (a) Mesh with distorted elements (tetrahedrons with zero or negative Jacobian are coloured in pink). (b) Edge ratio evaluation. For each mesh the average of the edge ratio of its elements vs. the standard deviation is plotted. The image-based pipeline meshes showed a better edge ratio. (c) For each mesh, the average of the minimum angle of each element vs. the standard deviation is plotted. The meshes created with the image-based pipeline showed higher minimum angle.

5 Appendix A

Supplementary data associated with this study can be found at <https://sites.google.com/site/serenabonaretti/>

References

1. Abaqus: ABAQUS/CAE user's manual : version 6.9.
2. Arsigny, V., Commowick, O., Pennec, X., Ayache, N.: A Log-Euclidean Framework for Statistics on Diffeomorphisms. In: Medical Image Computing and Computer-Assisted Intervention (MICCAI'06). vol. 9, pp. 924–31 (2006)
3. Boichon, C., Rochette, M., Schileo, E., Grassi, L., Taddei, F., Viceconti, M.: Shape Indexing of Human Femora Using Morphing and Principal Component Analysis. In: 1st Virtual Physiological Human Conference - VPH2010. No. 1 (2001)

4. Bonaretti, S., Reimers, N., Reyes, M., Nikitsin, A., Joensson, A., Nolte, L., Büchler, P.: Assessment of Peri-Articular Implant Fitting Based on Statistical Finite Element Modeling. In: MICCAI Workshop on Computational Biomechanics for Medicine III (2008)
5. Bredbenner, T.L., Eliason, T.D., Potter, R.S., Mason, R.L., Havill, L.M., Nicolella, D.P.: Statistical Shape Modeling Describes Variation in Tibia and Femur Surface Geometry between Control and Incidence Groups from the Osteoarthritis Initiative Database. *Journal of Biomechanics* 43(9), 1780–6 (2010)
6. Bryan, R., Mohan, P.S., Hopkins, A., Galloway, F., Taylor, M., Nair, P.B.: Statistical Modelling of the Whole Human Femur Incorporating Geometric and Material Properties. *Medical Engineering & Physics* 32(1), 57–65 (2010)
7. Cachier, P., Bardinet, E., Dormont, D., Pennec, X., Ayache, N.: Iconic Feature Based Nonrigid Registration: the PASHA Algorithm. *Computer Vision and Image Understanding* 89, 272–298 (2003)
8. Ciarelli, M.J., Goldstein, S.A., Kuhn, J.L., Cody, D.D., Brown, M.B.: Evaluation of Orthogonal Mechanical Properties and Density of Human Trabecular Bone from the Major Metaphyseal Regions with Materials Testing and Computed Tomography. *Journal of Orthopaedic Research* 9(5), 674–82 (1991)
9. Cootes, T., Taylor, C., Cooper, D., Graham, J.: Active Shape Models - Their Training and Application. *Computer Vision and Image Understanding* 61(1), 38–59 (1995)
10. Cootes, T.F., Taylor, C.J.: Statistical Models of Appearance for Medical Image Analysis and Computer Vision. In: *SPIE Medical Imaging*. pp. 236–248. Spie (2001)
11. Goodall, C.: Procrustes Methods in the Statistical Analysis of Shape. *Journal of the Royal Statistic society. Series B (Methodological)* 53(2), 285–339 (1991)
12. Helgason, B., Perilli, E., Schileo, E., Taddei, F., Brynjólfsson, S., Viceconti, M.: Mathematical Relationships between Bone Density and Mechanical Properties: A Literature Review. *Clinical Biomechanics* 23(2), 135–46 (2008)
13. Helgason, B., Taddei, F., Pálsson, H., Schileo, E., Cristofolini, L., Viceconti, M., Brynjólfsson, S.: A Modified Method for Assigning Material Properties to FE Models of Bones. *Medical Engineering & Physics* 30(4), 444–53 (2008)
14. Hraiech, N.: Mesh Morphing and Shape Indexing in Human Femur Modeling Applications. Ph.D. thesis (2010)
15. Hraiech, N., Taddei, F., Malvesin, E., Rochette, M., Viceconti, M.: Fast 3D Mesh Generation of Femur Based on Planar Parameterization and Morphing. In: *5th IEEE International Symposium on Biomedical Imaging: From Nano to Macro*. pp. 1561–1564. No. 3 (2008)
16. Keyak, J., Falkinstein, Y.: Comparison of In Situ and In Vitro CT Scan-based Finite Element Model Predictions of Proximal Femoral Fracture Load. *Medical Engineering & Physics* 25(9), 781–787 (2003)
17. Lorensen, W.E., Cline, H.E.: Marching Cubes: A High Resolution 3D Surface Construction Algorithm. *Computer Graphics* 21(4), 163–169 (1987)
18. Paulsen, R.R., Baerentzen, J.A., Larsen, R.: Markov Random Field Surface Reconstruction. *IEEE Transactions on Visualization and Computer Graphics* 16(4), 636–46 (2010)
19. Querol, L., Büchler, P., Rueckert, D., Nolte, L.: Statistical Finite Element Model for Bone Shape and Biomechanical Properties. In: *Medical Image Computing and Computer-Assisted Intervention (MICCAI'06)*. pp. 405 – 411 (2006)
20. Rueckert, D., Sonoda, L.I., Hayes, C., Hill, D.L., Leach, M.O., Hawkes, D.J.: Non-rigid Registration Using Free-Form Deformations: Application to Breast MR Images. *IEEE Transactions on Medical Imaging* 18(8), 712–21 (1999)

21. Rueckert, D., Frangi, A.F., Schnabel, J.a.: Automatic Construction of 3-D Statistical Deformation Models of the Brain Using Nonrigid Registration. *IEEE Transactions on Medical Imaging* 22(8), 1014–25 (2003)
22. Schileo, E., Dall’Ara, E., Taddei, F., Malandrino, A., Schotkamp, T., Baleani, M., Viceconti, M.: An Accurate Estimation of Bone Density Improves the Accuracy of Subject-Specific Finite Element Models. *Journal of Biomechanics* 41(11), 2483–91 (2008)
23. Schileo, E., Taddei, F., Cristofolini, L., Viceconti, M.: Subject-Specific Finite Element Models Implementing a Maximum Principal Strain Criterion Are Able to Estimate Failure Risk and Fracture Location on Human Femurs Tested In Vitro. *Journal of Biomechanics* 41(2), 356–67 (2008)
24. Schöberl, J.: NETGEN An Advancing Front 2D/3D-Mesh Generator Based on Abstract Rules. *Computing and Visualization in Science* 1, 41–52 (1997)
25. Schuler, B., Fritscher, K.D., Kuhn, V., Eckstein, F., Link, T.M., Schubert, R.: Assessment of the Individual Fracture Risk of the Proximal Femur by Using Statistical Appearance Models. *Medical Physics* 37(6), 2560–2571 (2010)
26. Seiler, C., Pennec, X., Ritacco, L., Reyes, M.: Femur Specific Polyaffine Model to Regularize the Log-Domain Demons Registration. In: *In SPIE Medical Imaging*. vol. 7962 (2011)
27. Vercauteren, T., Pennec, X., Perchant, A., Ayache, N.: Symmetric Log-Domain Diffeomorphic Registration: A Demons-based Approach. *Medical Image Computing and Computer-Assisted Intervention (MICCAI’08)* 11, 754–61 (2008)
28. Viceconti, M., Davinelli, M., Taddei, F., Cappello, A.: Automatic Generation of Accurate Subject-Specific Bone Finite Element Models to Be Used in Clinical Studies. *Journal of Biomechanics* 37(10), 1597–605 (2004)

Mesh-based vs. Image-based Statistical Appearance Model of the Human Femur: a Preliminary Comparison Study for the Creation of Finite Element Meshes – Supplementary Material

This file contains all the available information about the 196 femur CT image dataset.

The left part of the table refers to patient characteristics. The right part refers to image characteristics. At the bottom of the table, aggregate statistics can be found for both parts.

The orange labeled images failed either the mesh morphing or/and the image registration. The remaining 157 were used for the statistical model creation.

At present, data cannot be disclosed.

Id	Ethnicity	Gender	Age [yy]	Height [cm]	Weight [kg]	Tube voltage [kVp]	X-ray current [mA]	Pixel spacing [mm]	Slice thickness [mm]
1	ca	m	55	175	70	120	300	0.634	1.00
2	ca	m	69	167	82	120	300	0.782	1.00
3	ca	m	75	164	47	120	300	0.690	1.00
4	ca	m	75	180	70	120	300	0.782	1.00
5	ca	m	81	168	57	120	300	0.781	1.00
6	ca	f	24	162	57	120	300	0.782	1.00
7	ca	f	32	160	63	120	300	0.781	1.00
8	ca	f	42	157	52	120	300	0.735	1.00
9	ca	f	52	156	48	120	300	0.781	1.00
10	ca	f	66	150	50	120	300	0.735	1.00
11	ca	f	66	179	87	120	300	0.782	1.00
12	ca	f	77	160	50	120	300	0.686	1.00
13	ca	f	83	155	42	120	300	0.782	1.00
14	ca	f	87	155	65	120	300	0.782	1.00
15	ca	f	75	160	59	120	300	0.816	1.00
16	ca	f	48	169	70	120	300	0.858	1.00
17	ca	f	70	xxx	xxx	120	300	0.705	1.00
18	ca	f	56	170	75	120	300	0.682	1.00
19	ca	m	82	175	100	120	300	0.782	1.00
20	ca	f	63	165	65	120	300	1.087	1.00
21	ca	f	67	160	65	120	300	0.782	1.00
22	ca	f	56	168	90	120	300	0.781	1.00
23	ca	m	73	173	95	120	300	0.782	1.00

Id	Ethnicity	Gender	Age [yy]	Height [cm]	Weight [kg]	Tube voltage [kVp]	X-ray current [mA]	Pixel spacing [mm]	Slice thickness [mm]
24	ca	f	46	165	105	120	300	0.782	1.00
25	ca	f	82	165	50	120	300	0.610	1.00
26	ca	m	50	169	68	120	300	0.736	1.00
27	ca	m	60	178	75	120	300	0.923	1.00
28	ca	m	67	169	63	120	300	0.782	1.00
29	ca	f	76	160	78	120	300	0.782	1.00
30	ca	f	69	165	105	120	300	0.892	1.00
31	ca	m	75	173	75	120	300	0.751	1.00
32	ca	m	85	166	70	120	300	0.782	1.00
33	ca	f	77	160	60	120	300	0.736	1.00
34	ca	f	74	154	78	120	300	0.782	1.00
35	ca	m	83	170	70	120	300	0.782	1.00
36	ca	f	74	160	60	120	300	0.759	1.00
37	ca	m	58	168	67	120	300	0.782	1.00
38	ca	f	62	160	78	120	300	0.782	1.00
39	ca	f	69	162	55	120	300	0.755	1.00
40	ca	f	64	158	72	120	300	0.686	1.00
41	ca	f	52	168	80	120	300	0.808	1.00
42	ca	m	71	175	86	120	300	0.782	1.00
43	ca	f	86	162	59	120	300	0.755	1.00
44	ca	m	33	165	60	120	300	0.667	1.00
45	ca	m	30	170	70	120	300	0.705	1.00
46	ca	m	54	170	50	120	300	0.714	1.00
47	ca	m	71	180	120	120	300	0.892	1.00
48	ca	f	75	157	75	120	300	0.953	1.00
49	ca	f	67	178	83	120	300	0.877	1.00
50	ca	m	65	173	73	120	300	0.782	1.00
51	ca	f	50	162	74	120	300	0.782	1.00
52	ca	f	xxx	xxx	xxx	120	300	0.782	1.00
53	ca	m	23	166	55	120	300	0.709	1.00
54	ca	m	85	172	75	120	300	0.689	1.00
55	ca	m	51	175	62	120	300	0.782	1.00
56	ca	m	64	165	80	120	300	0.976	1.00
57	ca	f	xxx	xxx	xxx	120	300	0.782	1.00
58	ca	f	54	161	69	120	300	0.782	1.00
59	ca	m	67	154	52	120	300	0.625	1.00
60	ca	f	75	165	68	120	300	0.953	1.00
61	ca	m	34	172	90	120	300	0.984	1.00
62	ca	f	75	155	45	120	300	0.610	1.00

Id	Ethnicity	Gender	Age [yy]	Height [cm]	Weight [kg]	Tube voltage [kVp]	X-ray current [mA]	Pixel spacing [mm]	Slice thickness [mm]
63	ca	m	58	170	70	120	300	0.782	1.00
64	ca	f	85	167	50	120	300	0.782	1.00
65	ca	f	71	167	65	120	300	0.846	1.00
66	ca	m	53	164	60	120	300	0.877	1.00
67	as	m	67	170	65	120	300	0.782	1.00
68	ca	m	83	168	72	120	300	0.751	1.00
69	ca	f	48	156	80	120	300	0.782	1.00
70	as	m	59	172	82	120	300	0.781	1.00
71	as	f	51	172	82	120	300	0.781	1.00
72	ca	m	68	170	83	120	300	0.766	1.00
73	as	f	81	165	65	120	300	0.782	1.00
74	ca	m	79	166	55	120	300	0.888	1.00
75	ca	m	74	173	104	120	300	0.782	1.00
76	ca	m	68	168	68	120	300	0.782	1.00
77	ca	f	xxx	xxx	xxx	120	300	0.782	1.00
78	ca	f	81	160	72	120	300	0.782	1.00
79	ca	f	83	155	79	120	300	0.782	1.00
80	ca	m	78	170	60	120	300	0.652	1.00
81	ca	f	80	152	73	120	300	0.782	1.00
82	ca	m	63	166	57	120	300	0.782	1.00
83	af	m	60	170	70	120	300	0.938	1.00
84	ca	f	64	170	65	120	300	0.782	1.00
85	ca	f	21	165	65	120	300	0.782	1.00
86	ca	f	90	168	82	120	300	0.671	1.00
87	ca	m	84	180	90	120	300	0.782	1.00
88	ca	f	50	157	78	120	300	0.827	1.00
89	ca	f	81	162	52	120	300	0.782	1.00
90	ca	m	74	178	90	120	300	0.781	1.00
91	ca	m	45	xxx	xxx	120	300	0.781	1.00
92	ca	m	75	163	74	120	300	0.782	1.00
93	ca	f	76	160	62	120	300	0.781	1.00
94	ca	m	57	169	92	120	300	0.782	1.00
95	ca	f	72	160	65	120	300	0.782	1.00
96	ca	f	76	160	70	120	300	0.888	1.00
97	ca	f	63	175	74	120	300	0.896	1.00
98	ca	f	72	164	65	120	300	0.892	1.00
99	ca	f	78	165	90	120	300	1.060	1.00
100	ca	f	xxx	xxx	xxx	120	300	0.781	1.00
101	ca	f	48	163	140	120	300	1.171	1.00

Id	Ethnicity	Gender	Age [yy]	Height [cm]	Weight [kg]	Tube voltage [kVp]	X-ray current [mA]	Pixel spacing [mm]	Slice thickness [mm]
102	ca	f	52	157	65	120	300	0.782	1.00
103	ca	f	48	165	60	120	300	0.781	1.00
104	ca	f	78	160	50	120	300	0.881	1.00
105	ca	f	30	170	57	120	300	0.782	1.00
106	ca	m	73	180	76	120	300	0.740	1.00
107	as	m	xxx	xxx	xxx	120	xxx	0.836	1.00
108	as	m	xxx	xxx	xxx	120	xxx	0.764	1.00
109	as	m	xxx	xxx	xxx	120	xxx	0.732	1.00
110	as	m	xxx	xxx	xxx	120	xxx	0.762	1.00
111	as	m	xxx	xxx	xxx	120	xxx	0.734	1.00
112	as	m	xxx	xxx	xxx	120	xxx	0.680	1.00
113	as	m	xxx	xxx	xxx	120	xxx	0.684	1.00
114	as	m	xxx	xxx	xxx	120	xxx	0.736	1.00
115	as	m	46	xxx	xxx	120	xxx	0.781	1.00
116	as	m	53	xxx	xxx	120	xxx	0.684	1.00
117	as	m	42	xxx	xxx	120	xxx	0.684	1.00
118	as	m	57	xxx	xxx	120	xxx	0.781	1.00
119	as	m	29	165	65	120	xxx	0.684	1.00
120	as	m	30	xxx	xxx	120	xxx	0.684	1.00
121	as	m	69	168	78	120	xxx	0.684	1.00
122	as	f	68	xxx	xxx	120	xxx	0.684	1.00
123	as	m	68	166	61	120	xxx	0.684	1.00
124	as	f	71	xxx	xxx	120	xxx	0.684	1.00
125	as	m	64	xxx	xxx	120	xxx	0.781	1.00
126	as	m	63	xxx	xxx	120	xxx	0.684	1.00
127	as	m	74	xxx	xxx	120	xxx	0.684	1.00
128	as	f	73	xxx	xxx	120	xxx	0.684	1.00
129	as	m	70	xxx	xxx	120	xxx	0.684	1.00
130	as	f	74	xxx	xxx	120	xxx	0.684	1.00
131	ca	f	62	163	51	120	300	0.720	1.00
132	ca	m	43	175	84	120	300	0.766	1.00
133	ca	f	75	170	70	120	300	0.919	1.00
134	ca	f	58	xxx	xxx	120	300	0.907	1.00
135	ca	m	74	xxx	xxx	120	300	0.782	1.00
136	ca	f	65	xxx	xxx	120	300	0.782	1.00
137	ca	f	43	168	75	120	300	0.735	1.00
138	ca	m	84	xxx	xxx	120	300	0.782	1.00
139	ca	f	90	170	74	120	300	0.782	1.00
140	ca	m	55	172	67	120	300	0.662	1.00

Id	Ethnicity	Gender	Age [yy]	Height [cm]	Weight [kg]	Tube voltage [kVp]	X-ray current [mA]	Pixel spacing [mm]	Slice thickness [mm]
141	af	f	69	160	85	xxx	xxx	0.846	1.00
142	ca	m	87	181	88	120	300	0.782	1.00
143	ca	m	40	171	82	120	300	0.714	1.00
144	as	f	50	158	63	120	300	0.782	1.00
145	ca	m	69	173	96	120	300	0.782	1.00
146	ca	f	58	164	64	120	300	0.782	1.00
147	ca	m	74	170	92	120	300	0.781	1.00
148	ca	m	56	180	93	120	300	0.782	1.00
149	ca	f	60	160	50	120	xxx	0.625	1.00
150	ca	f	43	175	80	120	xxx	0.663	1.00
151	ca	f	84	160	55	120	xxx	0.892	1.00
152	ca	m	81	160	80	120	400	0.827	1.00
153	ca	f	66	155	100	120	400	0.782	1.00
154	ca	f	73	160	65	120	300	0.782	1.00
155	af	m	64	164	67	xxx	xxx	0.782	1.00
156	ca	m	81	170	80	120	300	0.782	1.00
157	ca	f	46	168	58	120	xxx	0.781	1.00
158	ca	f	72	163	90	135	350	0.923	1.00
159	ca	f	65	163	68	120	xxx	0.744	1.00
160	af	m	74	165	72	120	300	0.782	1.00
161	ca	m	68	165	75	120	xxx	0.782	1.00
162	af	f	37	160	75	120	120	0.782	1.00
163	ca	m	51	159	67	120	xxx	0.782	1.00
164	ca	m	74	167	50	120	xxx	0.720	1.00
165	ca	f	69	xxx	xxx	120	xxx	0.709	1.00
166	ca	m	75	180	68	120	350	0.782	1.00
167	ca	m	57	179	110	120	xxx	0.877	1.00
168	ca	m	64	170	57	120	xxx	0.782	1.00
169	af	f	79	160	80	xxx	xxx	0.820	1.00
170	ca	f	74	174	74	120	350	0.843	1.00
171	ca	m	78	166	60	120	350	0.782	1.00
172	ca	f	81	163	59	120	350	0.686	1.00
173	ca	f	71	169	67	120	300	0.766	1.00
174	ca	m	68	175	110	120	300	0.949	1.00
175	ca	m	55	174	84	120	350	0.782	1.00
176	ca	f	65	160	66	120	xxx	0.843	1.00
177	ca	m	65	180	55	120	xxx	0.782	1.00
178	ca	m	66	175	57	120	250	0.782	1.00
179	ca	f	74	155	99	120	350	1.049	1.00

Id	Ethnicity	Gender	Age [yy]	Height [cm]	Weight [kg]	Tube voltage [kVp]	X-ray current [mA]	Pixel spacing [mm]	Slice thickness [mm]
180	ca	f	39	175	72	120	xxx	0.782	1.00
181	ca	f	72	160	70	120	xxx	0.877	1.00
182	ca	f	93	165	50	120	350	0.782	1.00
183	ca	m	76	157	67	120	350	0.782	1.00
184	ca	f	76	151	63	120	350	0.782	1.00
185	af	f	26	160	60	120	350	0.782	1.00
186	ca	m	50	170	70	120	350	0.724	1.00
187	ca	f	47	170	50	120	350	0.735	1.00
188	ca	f	74	160	90	120	350	0.824	1.00
189	ca	f	30	165	50	120	350	0.723	1.00
190	ca	f	56	157	57	120	xxx	0.675	1.00
191	ca	f	35	175	62	120	xxx	0.675	1.00
192	ca	m	64	168	72	120	350	0.782	1.00
193	ca	m	62	165	110	120	xxx	0.938	1.00
194	ca	f	77	160	61	120	250	0.751	1.00
195	ca	f	71	160	73	120	xxx	0.782	1.00
196	ca	f	81	165	83	120	xxx	0.782	1.00

Data characteristics:

Patient data:

Ethnicity

Caucasian:	160
Asian:	28
African:	7

Gender

Male:	92
Female:	104

Age [yy]

Average:	64.3261
Std dev:	15.4014
Data available:	184
Data not available (xxx):	12

Height [cm]

Average:	166.0854
Std dev:	6.9630
Data available:	164
Data not available (xxx):	32

Weight [kg]

Average:	71.4268
Std dev:	15.7947
Data available:	164
Data not available (xxx):	32

Image characteristics:

Tube voltage [kVp]

Min:	120
Max:	135
Data available:	193
Data not available (xxx):	3

X-ray current [mA]

Min:	120
Max:	400
Data available:	149
Data not available (xxx):	47

Pixel spacing [mm]

Min:	0.610
Max:	1.171

Slice thickness [mm]

Min:	1.00
Max:	1.00

Mesh-based vs. Image-based Statistical Appearance Model of the Human Femur: a Preliminary Comparison Study for the Creation of Finite Element Meshes – Supplementary Material

This file contains a schematic list of the main formulas and parameters used in this study. ITK 3.20 and VTK 5.6.1 classes and the additional tools are specified; where not mentioned differently, home-made code was used. The steps in brackets in the following section titles refer to Figure 1 in the main paper, which is reported here for completeness.

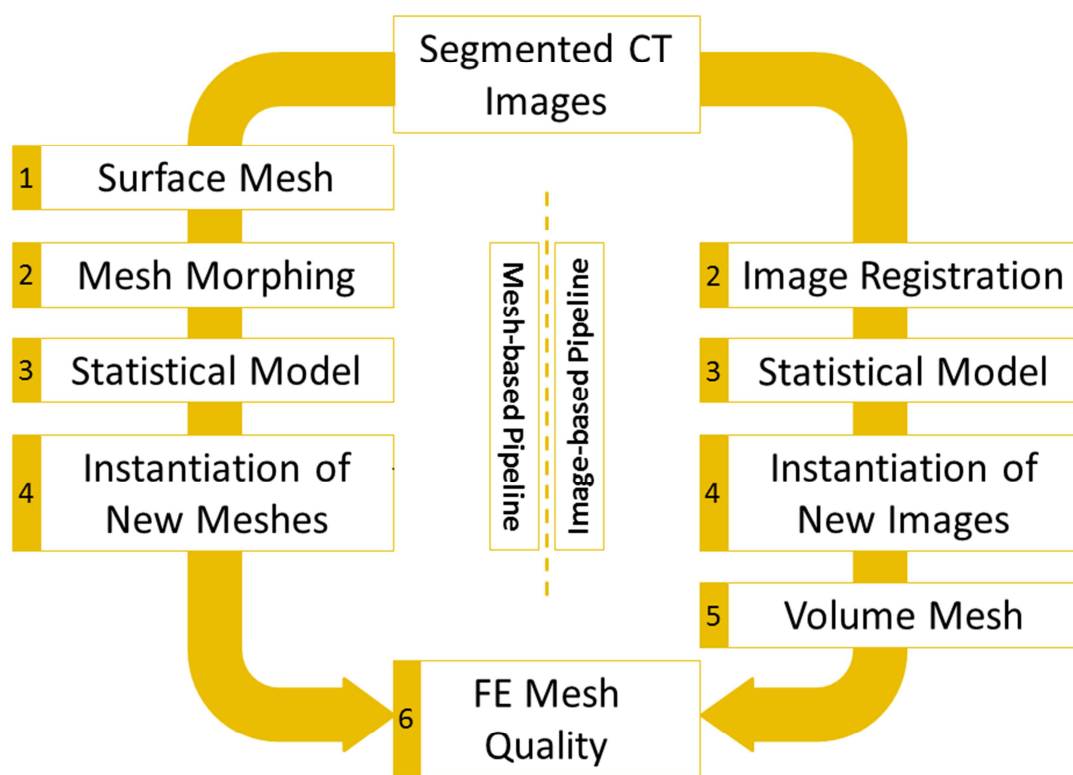


Fig. 1: Mesh-based and image-based statistical appearance model pipelines for the creation of femur finite element meshes. On the left side, the steps for the mesh-based approach are shown, whereas on the right side the steps for the image-based pipeline are depicted.

SEGMENTED CT IMAGES

- See file: Appendix A - dataset.pdf

FEM MESH CREATION PARAMETERS (step 1 and step 5)

Surface mesh creation:

- Marching cubes (`vtkMarchingCubes`)
 - o thresholded on the bone segmentation mask
- Simplification (`vtkDecimatePro`):
 - o Reduction parameter: 0.4
- Smoothing (`vtkSmoothPolyDataFilter`):
 - o Number of iterations: 150
- Topology recreation:
 - o MRFSurface (<http://www2.imm.dtu.dk/image/MRFSurface/>)

Volume mesh creation:

- NetGen (<http://sourceforge.net/projects/netgen-mesher/>) parameters:
 - o Mesh granularity: very fine
 - o Element order: second
 - o Max mesh-size: 500
 - o Min mesh-size: 500
 - o Mesh-size grading: 0.1

MESH MORPHING PARAMETERS (step 2)

- Information cannot be disclosed.

IMAGE REGISTRATION PARAMETERS (step 2)

- Rigid alignment:
 - o Alignment and centering of bounding boxes that enclose the surface obtained from image masks through marching cubes (`vtkMarchingCubes`)
- Log-Domain Demons (<http://www.insight-journal.org/browse/publication/644>):
 - o Default parameters
- Extension of Log-Domain Demons code for polyaffine regularization:
 - o 3 regions: head, shaft and condyles after rigid alignment
 - o Gaussian function for spatial weighting of each region is set to $\mu = 0$ and $\sigma = 0.125$
 - o Along the transversal axis the positions are set to achieve an equal weighting at the boundary of two adjacent regions

STATISTICAL MODELS (step 3)

- Mesh-based approach: alignment using the Procrustes algorithm (`vtkProcrustesAlignmentFilter`)
- Shape PCA
 - o $x = \bar{x} + \Phi_s b_s$
 - o Mesh-based pipeline: (`vtkPCAAnalysisFilter`)
 - o Image-based pipeline: (extension of the class `itkImagePCAShapeModelEstimator` for vector images)
- Intensity PCA:
 - o $g = \bar{g} + \Phi_g b_g$
 - o Image-based pipeline: (`itkImagePCAShapeModelEstimator`)
- Combined PCA:
 - o $b = \begin{pmatrix} w_s b_s \\ b_g \end{pmatrix} = \begin{pmatrix} w_s \Phi_s^T (x - \bar{x}) \\ \Phi_g^T (g - \bar{g}) \end{pmatrix}$
where $w_s = rI$, $r = \sqrt{\frac{\sum \lambda_g}{\sum \lambda_s}}$, I is the identity matrix

NEW INSTANCES CREATION (step 4)

- Shape: $\tilde{x} = \bar{x} + \Phi_s W_s^{-1} \Phi_{c,s} c$, $-2\sqrt{\lambda_i} \leq c \leq +2\sqrt{\lambda_i}$
- Intensity: $\tilde{g} = \bar{g} + \Phi_g \Phi_{c,g} c$

FE MESH QUALITY ASSESSMENT (step 6)

- Computation of Jacobian, edge ratio and minimum angle (`vtkMeshQuality`) for each mesh elements. Threshold criteria from “Abaqus/CAE user’s manual”, version 6.9, cap. 17.6.1.
Exclusion of meshes whose elements have:
 - o Jacobian ≤ 0.0001
 - o Edge ratio ≥ 10
 - o Minimum angle $\leq 5^\circ$